

# An isotopically distinct Zealandia–Antarctic mantle domain in the Southern Ocean

Sung-Hyun Park<sup>1\*</sup>, Charles H. Langmuir<sup>2</sup>, Kenneth W. W. Sims<sup>3</sup>, Janne Blichert-Toft<sup>4</sup>, Seung-Sep Kim<sup>5</sup>, Sean R. Scott<sup>3</sup>, Jian Lin<sup>6,7</sup>, Hakkyum Choi<sup>1</sup>, Yun-Seok Yang<sup>1</sup> and Peter J. Michael<sup>8</sup>

**The mantle sources of mid-ocean ridge basalts beneath the Indian and Pacific oceans have distinct isotopic compositions with a long-accepted boundary at the Australian–Antarctic Discordance along the Southeast Indian Ridge. This boundary has been widely used to place constraints on large-scale patterns of mantle flow and composition in the Earth’s upper mantle. Sampling between the Indian and Pacific ridges, however, has been lacking, especially along the remote 2,000 km expanse of the Australian–Antarctic Ridge. Here we present Sr, Nd, Hf and Pb isotope data from this region that show the Australian–Antarctic Ridge has isotopic compositions distinct from both the Pacific and Indian mantle domains. These data define a separate Zealandia–Antarctic domain that appears to have formed in response to the deep mantle upwelling and ensuing volcanism that led to the break-up of Gondwana 90 million years ago, and currently persists at the margins of the Antarctic continent. The relatively shallow depths of the Australian–Antarctic Ridge may be the result of this deep mantle upwelling. Large offset transforms to the east may be the boundary with the Pacific domain.**

Isotopic compositions of oceanic basalts constrain mantle composition, evolution and convective flow<sup>1,2</sup>. Basalts from Indian mid-ocean ridges, for example, have higher <sup>208</sup>Pb/<sup>204</sup>Pb at a given <sup>206</sup>Pb/<sup>204</sup>Pb than those from the East Pacific Rise (EPR) and the Pacific–Antarctic Ridge (PAR)<sup>3–5</sup>. Also, the Indian ridges are distinguished by having higher <sup>176</sup>Hf/<sup>177</sup>Hf for a given <sup>143</sup>Nd/<sup>144</sup>Nd (refs. <sup>5,6</sup>). These isotopic differences imply the existence of ocean-scale upper-mantle domains with limited interactions over long periods of time<sup>7–9</sup>, and raise the question of the location of their boundaries. In the present case, the Australian–Antarctic Discordance (AAD) was proposed to be the boundary between the Indian and Pacific mantle domains because it constitutes a remarkably deep portion of the global mid-ocean ridge system that demarks abrupt changes in isotopic ratios from Indian to Pacific values. There remained, however, a broad gap in sampling between the AAD and the Pacific ridges to the east, which leaves the definitiveness of the boundary in question. In their study of the PAR, Vlastélic et al.<sup>4</sup> demonstrated that the Pacific upper mantle is not homogeneous, but consists of two distinct subdomains separated by the Pacific Superswell. However, this finding did not bring resolution to the unsettled demarcation of the striking isotopic contrast between the Indian and Pacific mantle domains.

The last gap in the mapping and sampling of seafloor spreading centres worldwide was the Australian–Antarctic Ridge (AAR), a 2,000 km expanse in the most remote parts of the ocean ridge system. The collection and isotopic measurements of samples from the AAR provide answers to two key questions. Does the AAR, which lies to the east of the AAD, have a composition as predicted akin to that of the Pacific? And is the AAD the major boundary between the Pacific and Indian suboceanic mantle domains? We show here that “no” is the answer to both questions. Instead, our new data reveal the existence of a new mantle domain and constrain its origin.

## Expeditions to terra incognita

In 2011 and 2013, the Korean icebreaker RV *Aaron* conducted three scientific expeditions to map and sample two segments in the middle of the AAR—KR1 and KR2 (Fig. 1). These cruises provided the first samples and detailed mapping of the remote AAR, and filled an important gap in our knowledge of the crust and mantle in this region.

The KR1 and KR2 segments have intermediate spreading rates of ~70 mm yr<sup>-1</sup>. Segment KR1 is a 300 km long supersegment (Fig. 1a) that exhibits large along-axis topographic differences from 1,800 to 2,800 m. The axial depth and morphology of KR1 vary from west to east, and range from an axial plateau in the westernmost region to an axial rift, a narrow axial high, a flat axis and finally a well-developed rift valley in the easternmost region (Fig. 1b). Segment KR2, located northwest of KR1, has a western axial high and eastern rift valley. These segments exhibit shallower axial depths (1,800–2,800 m) than the mean axial depth (3,000 m) of ocean ridges of intermediate spreading rates<sup>10</sup>.

## A unique isotopic signature in the Southern Ocean

The isotopic compositions of Sr, Nd, Hf and Pb for the KR1 and KR2 ridge segments are listed in Supplementary Data Table 1. <sup>206</sup>Pb/<sup>204</sup>Pb values for KR1 vary between 18.7 and 19.1 from the west to the middle of the segment and gradually decrease eastward to ~18.4 (Fig. 1c). <sup>206</sup>Pb/<sup>204</sup>Pb values for KR2 are ~18.4, except for the westernmost sample which has a value of 19.2. Relative variations in the Hf isotopic compositions (expressed here as  $\epsilon_{\text{Hf}} = +12.8$  to  $+18.3$ ) are almost a mirror image of the <sup>206</sup>Pb/<sup>204</sup>Pb along-axis variations (Fig. 1d).  $\epsilon_{\text{Nd}}$  varies from +7.4 to +10.1 and is well correlated ( $R^2 = 0.93$ ) with  $\epsilon_{\text{Hf}}$ .  $\epsilon_{\text{Hf}}$  to the east of 159° 50' E is very high (up to  $+18.3$ ) compared to the majority of Pacific-type depleted mantle (up to  $+17$ )<sup>6,11</sup>. In contrast,

<sup>1</sup>Korea Polar Research Institute, Incheon, Republic of Korea. <sup>2</sup>Department of Earth and Planetary Sciences, Harvard University, Cambridge, MA, USA.

<sup>3</sup>Department of Geology and Geophysics, University of Wyoming, Laramie, WY, USA. <sup>4</sup>Laboratoire de Géologie de Lyon, Ecole Normale Supérieure de Lyon and Université Claude Bernard Lyon 1, CNRS UMR 5276, Lyon, France. <sup>5</sup>Department of Geology and Earth Environmental Sciences, Chungnam National University, Daejeon, Republic of Korea. <sup>6</sup>Department of Geology and Geophysics, Woods Hole Oceanographic Institution, Woods Hole, MA, USA.

<sup>7</sup>Key Laboratory of Ocean and Marginal Sea Geology, South China Sea Institute of Oceanography, Chinese Academy of Sciences, Guangzhou, China.

<sup>8</sup>Department of Geosciences, University of Tulsa, Tulsa, OK, USA. \*e-mail: [shpark314@kopri.re.kr](mailto:shpark314@kopri.re.kr)

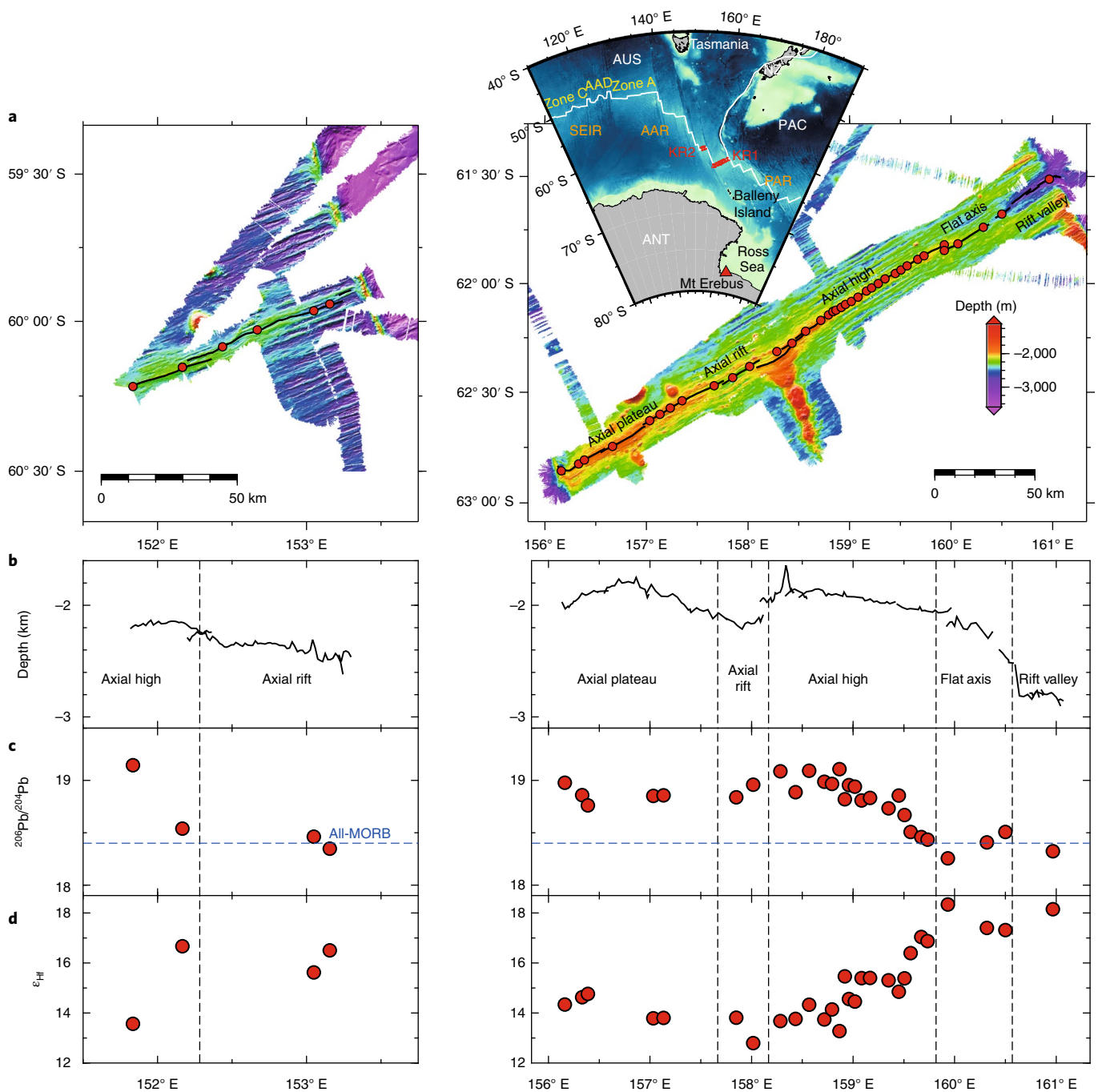


**Fig. 1 | Bathymetry and along-axis variations in depth,  $^{206}\text{Pb}/^{204}\text{Pb}$  and  $\epsilon_{\text{Hf}}$  for the KR1 and KR2 segments of the AAR. **a**, Bathymetric maps for the KR1 (right) and KR2 (left) segments were produced using multibeam echo sounder data (Kongsberg EM122) acquired during three Korean Polar Ridge program (KOPRIDGE) cruises. Inset: important tectonic features in the vicinity of the AAR. Circles show the sampling locations of the wax corer. These maps indicate that the AAR mainly consists of a series of first-order segments bounded by parallel transform faults. ANT, Antarctic Plate; AUS, Australian Plate; PAC, Pacific Plate; NZ, New Zealand. **b**, The KR1 segment (right) is a 300-km-long supersegment that exhibits large topographic variation from west to east: an axial plateau in the west, followed by an axial rift, a narrow axial high, a flat axis and a well-developed rift valley. The KR2 segment (left) also shows topographic variation with a western axial high and an eastern rift valley. Both segments are shallower than the mean axial depth of global mid-ocean ridges, which implies a more buoyant mantle beneath the KR1 and KR2 segments<sup>43</sup>. **c**, All-MORB (mid-ocean ridge basalts) indicates the total composition of the crust excluding back-arc basins<sup>10</sup>. Most of the KR1 and KR2 samples have higher  $^{206}\text{Pb}/^{204}\text{Pb}$  than All-MORB, which suggests they are enriched compared to the global average. The variation of  $^{206}\text{Pb}/^{204}\text{Pb}$  (18.3–19.1) is comparable to that of the Galapagos Spreading Centre, which suggests the KR1 and KR2 segments are supplied by heterogeneous mantle as for ridges that interact with a plume<sup>30</sup>. **d**, The  $\epsilon_{\text{Hf}}$  variation of the KR1 (right) and KR2 (left) segments (about +12.8 to +18.3) is comparable to that of the Galapagos Spreading Centre (about +9 to +16)<sup>12,50</sup>. However, the  $\epsilon_{\text{Hf}}$  of the KR1 and KR2 extends to higher values than the Galapagos data, which suggests the mantle beneath the KR1 and KR2 segments is more depleted than the Galapagos mantle.**

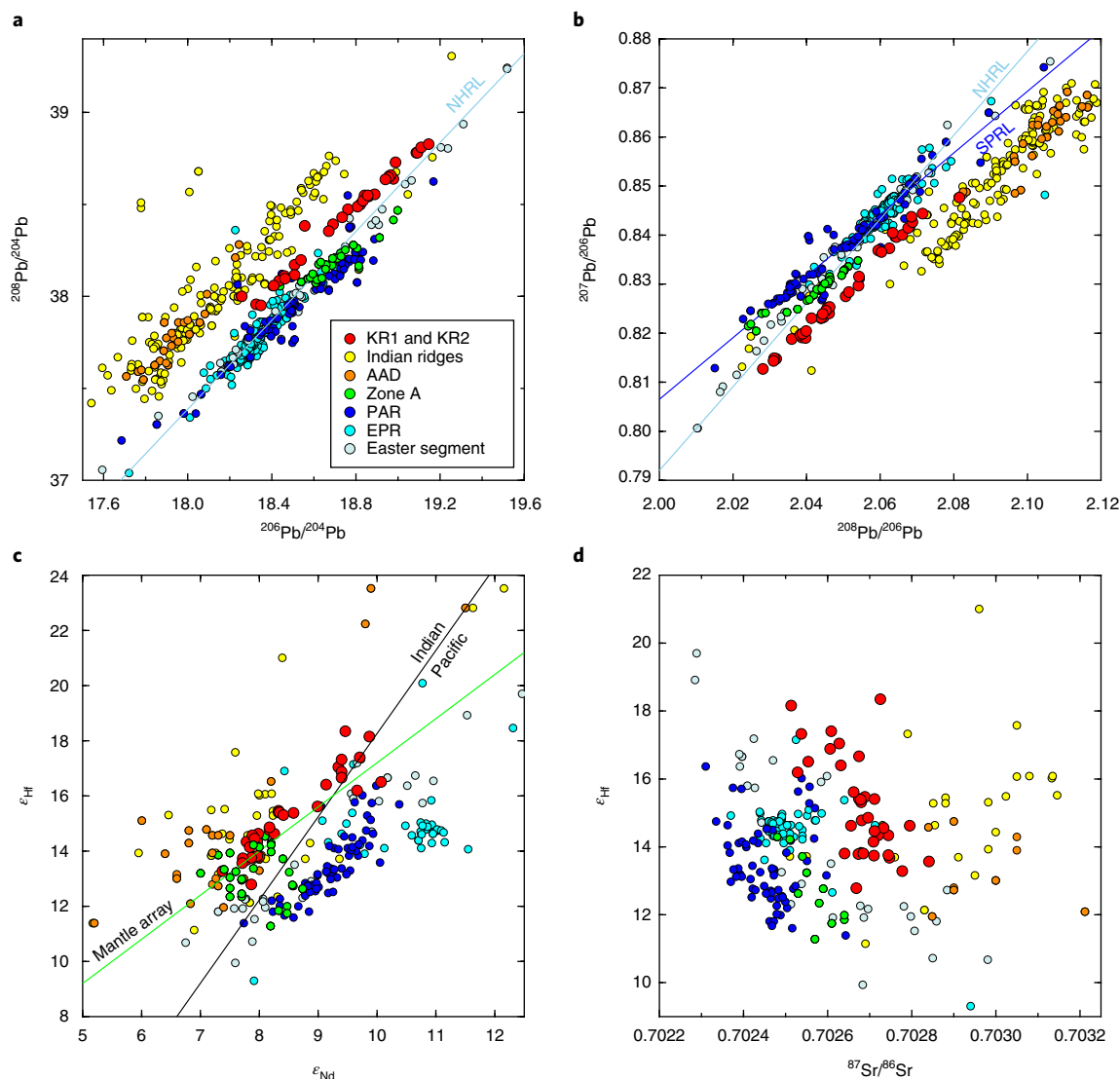


**Fig. 2 | Comparisons of isotope ratios from the KR1 and KR2 segments and other mid-ocean ridge basalts.** Available isotope data from the Indian ridges, AAD, Zone A, PAR, EPR and the Easter segment are compared with the KR1 and KR2 segments. The data are mostly from Gale et al.<sup>10</sup> and references therein. Data from Hanan et al.<sup>51</sup> are added for the Indian ridges. PAR data are from Vlastélic et al.<sup>4</sup> and Hamelin et al.<sup>52</sup>. **a**, The KR1 and KR2 segment data plot above the Northern Hemisphere reference line (NHRL)<sup>12</sup>. At a given  $^{206}\text{Pb}/^{204}\text{Pb}$ , the PAR data mostly plot below the NHRL, on a trend with shallower slope. **b**, The SPRL is estimated as  $^{207}\text{Pb}/^{206}\text{Pb} = 0.6253 \times (^{208}\text{Pb}/^{206}\text{Pb}) - 0.4441$  with  $R^2 = 0.92$ . The slope of SPRL is shallower than that of the NHRL (see the EPR samples), which supports the hypothesis that the northern and southern Pacific mantle domains are isotopically distinct. **c**, The mantle array is defined as  $\epsilon_{\text{Hf}} = 1.59\epsilon_{\text{Nd}} + 1.28$  (ref. 53). The dividing line for the Indian and Pacific mantle domains is from Kempton et al.<sup>5</sup>. The KR1 and KR2 data mostly fall within the Indian mantle domain. In addition, the KR1 and KR2 samples have a higher  $\epsilon_{\text{Hf}}$  than the mantle array for a given  $\epsilon_{\text{Nd}}$ , whereas the PAR and EPR plot below the mantle array. **d**, Clear separations between the EPR, PAR, KR1 and KR2 segments, Zone A and Indian MORB are evident. At a given  $\epsilon_{\text{Hf}}$ , the PAR is the lowest in  $^{87}\text{Sr}/^{86}\text{Sr}$ , the EPR the second lowest, the KR1 and KR2 segments the third lowest and the Indian MORB the highest. At a given  $\epsilon_{\text{Hf}}$ , Zone A is slightly higher in  $^{87}\text{Sr}/^{86}\text{Sr}$  than the PAR, yet lower than the KR1 and KR2 segments. Zone A is closer to the KR1 and KR2 segments in Pb isotope composition and  $\epsilon_{\text{Hf}}$  and  $\epsilon_{\text{Nd}}$ , but different for  $\epsilon_{\text{Hf}}$  and  $^{87}\text{Sr}/^{86}\text{Sr}$ , which suggests that Zone A differs from both the KR1 and KR2 segments and PAR. Thus, Zone A is no longer considered as belonging to the Pacific mantle. However, it appears that Zone A and the KR1 and KR2 segments share a similar depleted component.

the middle of KR1 is relatively enriched, with a high  $^{206}\text{Pb}/^{204}\text{Pb}$  and low values of  $\epsilon_{\text{Nd}}$  and  $\epsilon_{\text{Hf}}$ . Note that KR1 encompasses essentially the full range of  $\epsilon_{\text{Hf}}$  values for Pacific mid-ocean ridge basalts (MORB) in just one segment. KR2 has  $\epsilon_{\text{Hf}}$  values from +15.6 to +16.7 and  $\epsilon_{\text{Nd}}$  values from +9.0 to +10.1 except for the westernmost sample, for which  $\epsilon_{\text{Hf}}$  is +13.6 and  $\epsilon_{\text{Nd}}$  is +7.7. The combined isotopic ratios of Sr, Nd, Hf and Pb permit a robust comparison of the KR1 and KR2 segments with the Indian and Pacific ridges (Figs. 1 and 2), and show that the former are distinct from both the neighbouring

Pacific and Indian mantle compositions. At a given  $^{206}\text{Pb}/^{204}\text{Pb}$ , the KR1 and KR2 samples have higher  $^{208}\text{Pb}/^{204}\text{Pb}$  than Pacific samples, and lower  $^{208}\text{Pb}/^{204}\text{Pb}$  than Indian samples (Fig. 2a). An effective discriminant is  $\Delta 8/4$ , which is the magnitude of the  $^{208}\text{Pb}/^{204}\text{Pb}$  divergence from a regression line based on Northern Hemisphere samples<sup>12</sup> (Fig. 2a). The KR1 and KR2 segments have  $\Delta 8/4$  of +10 to +18, higher than both the PAR (−30 to +10) and EPR (−10 to +10), but lower than the Indian ridges (greater than +22 and up to +80) (Fig. 3a). At a given  $^{208}\text{Pb}/^{206}\text{Pb}$ , all the KR1 and KR2 samples have

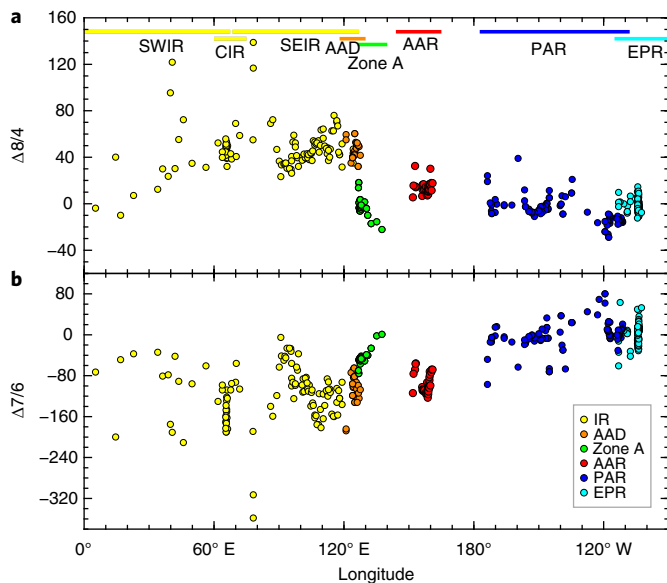


**Fig. 3 |  $\Delta 8/4$  and  $\Delta 7/6$  variations.** **a, b**, Variations in the  $\Delta 8/4$  (**a**) and  $\Delta 7/6$  (**b**) values for samples collected along mid-ocean ridges and plotted as a function of longitude.  $\Delta 7/6$  is defined as  $[(^{207}\text{Pb}/^{206}\text{Pb})_{\text{sample}} - (^{207}\text{Pb}/^{206}\text{Pb})_{\text{SPRL}}] \times 10^4$ . CIR, Central Indian Ridge; SEIR, Southeast Indian Ridge; SWIR, Southwest Indian Ridge; IR, Indian ridges.

lower  $^{207}\text{Pb}/^{206}\text{Pb}$  values than those of Pacific samples (Fig. 2b). Another powerful discriminant is  $\Delta 7/6$ , which is the deviation of a given sample from a southern Pacific reference line (SPRL) defined here as the best fit to the  $^{207}\text{Pb}/^{206}\text{Pb}$ – $^{208}\text{Pb}/^{206}\text{Pb}$  variations of the PAR based on the least squares method (Fig. 2b). The  $\Delta 7/6$  of PAR samples is between  $-10$  and  $+10$ , whereas KR1 and KR2 segments show negative values between  $-70$  and  $-120$  (Figs. 2b and 3b). The KR1 and KR2 segments also plot on the Indian side of the 'Indian/Pacific' dividing line in  $\epsilon_{\text{Nd}}-\epsilon_{\text{Hf}}$  space (Fig. 2c)<sup>5</sup>, whereas at a given value of  $\epsilon_{\text{Hf}}$  the KR1 and KR2 samples have Sr isotope compositions intermediate to those of the Pacific and Indian ridges (Fig. 2d). These differences demonstrate that the KR1 and KR2 segments have a unique isotopic signature that is distinct from both Pacific and Indian ridge samples.

Comparison with other data in the region suggests a widespread distribution of this distinctive composition (Figs. 4 and 5a). Volcanic samples from Ross Island<sup>13,14</sup>, the West Antarctic Rift System (WARS)<sup>15–18</sup>, Balleny and Scott Islands<sup>19</sup>, Macquarie Island<sup>20</sup> and Zealandia<sup>21–24</sup> exhibit coherent relationships with the KR1 and KR2 segments (Fig. 4). The data are consistent with mixing an enriched component with high Pb isotope ratios akin to high- $\mu$  (HIMU), found almost ubiquitously in the region's Cenozoic alkaline volcanic rocks, with a depleted mantle component distinct from both the Pacific and Indian suboceanic mantle domains. Although most of the regional Cenozoic alkaline volcanism was not derived from an ocean ridge, it is still isotopically coherent with the AAR samples. For example, the active Mt Erebus and neighbouring volcanoes on Ross Island, which are part of the WARS<sup>13,14</sup> and hence of the same isotopic grouping, display the same mixing relationship between an old enriched HIMU-like component sourced in the deep mantle and the depleted upper mantle, which thereby defines a mixing zone (Fig. 5a).

The geographical limits of this mixing zone can be delineated based on the isotopic compositions of lavas from Marie Byrd Land<sup>25,26</sup>, East Australia<sup>27–31</sup> and Zone A. The Marie Byrd Land and East Australia samples show slightly different trends from those of the KR1 and KR2 segments in multi-isotope space

(Fig. 4), which suggests that the mixing zone does not extend to these regions.

Zone A to the east of the AAD was previously considered to be the geographical beginning of the Pacific mantle domain<sup>5–7</sup>, but this view is now no longer supported by the currently available isotope data. Zone A samples are distinct from the Indian ridge samples to the west (Figs. 2–4) and Pacific samples to the east, being intermediate in composition to the new AAR data reported here and data from the EPR and PAR. The margin between Zone A and the KR2 segment establishes the western boundary of the mixing zone (thick black dashed lines in Fig. 5a). To determine more precisely the extent and characteristics of the mixing zone will require future systematic sampling between the east of the KR1 segment and the PAR, and between Zone A and the west of the KR2 segment (data gaps in Fig. 5a).

All the samples between Zone A and the west end of the PAR fall below the SPRL with negative  $\Delta 7/6$  values. This region (inside the pink dashed lines in Fig. 5a) is entirely distinct from both the Indian and Pacific mantle domains as apparent from the discrete clusters in  $\Delta 7/6$ – $\Delta 8/4$  space as a function of longitudinal position (Figs. 3 and 5b). The large expanse in both space and time is consistent with an extensive, distinct mantle domain, for which we propose the name 'Zealandia–Antarctic Swell'. The presence of this new mantle domain indicates that the AAD is not, as previously thought, the boundary between the Indian and Pacific suboceanic mantles. It remains, however, the boundary of the Indian Ocean domain.

### Origin and dynamics of the Zealandia–Antarctic Swell

From the coherency in isotopic characteristics between the AAR and other volcanic rocks from neighbouring regions (Mt Erebus, Ross Island, WARS and so on), we propose that the Zealandia–Antarctic domain was initiated by the superplume associated with the break-up of Gondwana<sup>32,33</sup>. Subsequent active mantle upwelling in the region includes both rifting, as represented by the AAR, and asthenospheric channelling from present-day plumes, such as Balleny and Ross Islands<sup>14,34,35</sup>.

The plume model is supported by the isotopic compositions of the Hikurangi Seamounts. The Hikurangi data lie along the mixing trajectories that connect the AAR and surrounding regions (Fig. 4). For example, the  $\epsilon_{\text{Nd}}-\epsilon_{\text{Hf}}$  diagram (Fig. 4c) shows that the isotopic variations of Hikurangi and WARS samples are better explained by mixing with the depleted KR1 and KR2 component than with the PAR source. Deviation of the Hikurangi Seamounts and some Zealandia samples from the mixing relationship in Nd–Pb isotope space may be due to contamination by subcontinental lithospheric mantle (Fig. 4d)<sup>32</sup>, which is often observed in volcanic rocks erupted during initial stages of rifting. The Hikurangi Seamounts were formed by the superplume that resulted in the break-up of New Zealand and Antarctica at  $\sim 90$  Ma<sup>32,33</sup>. Based on plate reconstruction models<sup>36</sup>, the Hikurangi Seamounts erupted at locations similar to those of the KR1 and KR2 segments at  $\sim 90$  Ma, which implies that this particular mantle domain may be associated with the onset of the New Zealand and Antarctica break-up caused by the superplume<sup>32,33</sup>.

Alternatives to the plume model have been put forward by other studies that suggest the enriched component may be derived from the overriding continental lithosphere contaminated by the subduction of the Pacific and Phoenix plates<sup>18,37</sup>. This metasomatically enriched lithospheric mantle model<sup>18,37</sup>, however, cannot explain the isotopic coherence among the KR1 and KR2 segments, Ross Island and the Hikurangi Seamounts (Fig. 4c). As the Hikurangi Seamounts erupted on the oceanic lithosphere subducting along the former Gondwana margin<sup>32,38</sup>, the compositional influence of the subcontinental material on the Hikurangi volcanism would be minimal. Moreover, it is physically implausible that the lithospheric material could influence midocean ridge volcanism 800 km away from both

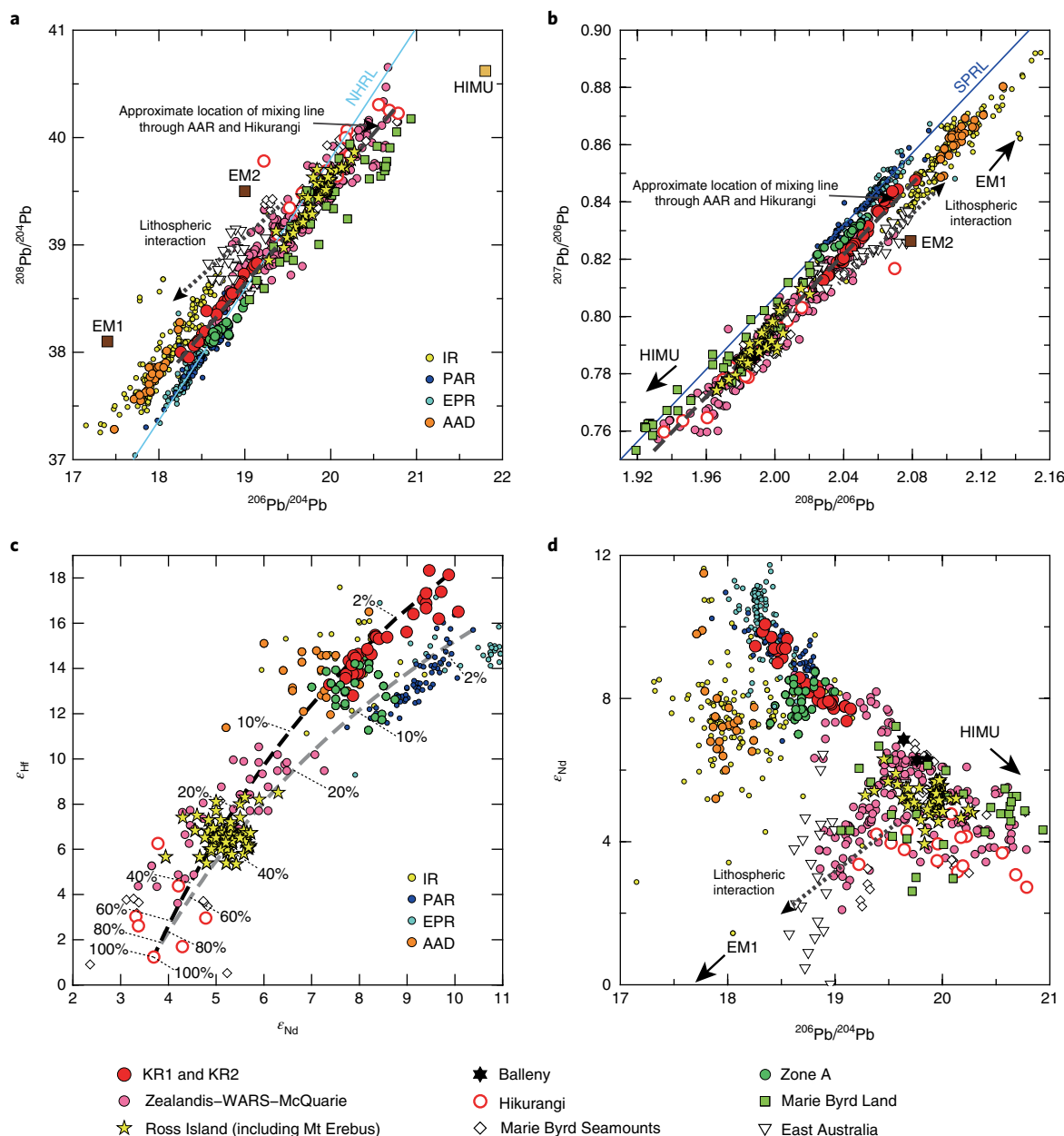


**Fig. 4 | Comparison of isotope ratios from KR1 and KR2 with Gondwana margin locations (Zealandia, WARS, Balleny and Scott Islands, Marie Byrd Land and East Australia).** **a**, The WARS, which includes Ross Island (and Mt Erebus), Balleny and Scott Islands, Macquarie Island and Zealandia, lies on the same mixing line as the KR1 and KR2 segments as do the Hikurangi Seamounts that erupted during the initial stages of rifting of New Zealand and Antarctica at -90 Ma during the break-up of Gondwana. In contrast, Marie Byrd Land and Zone A define a different slope relative to the KR1 and KR2 segments and to East Australia. EM1, enriched mantle 1; EM2, enriched mantle 2; HIMU, high- $\mu$  ( $^{238}\text{U}/^{204}\text{Pb}$ ). **b**, The data from the Hikurangi Seamounts, Zealandia, the WARS and Balleny and Scott Islands lie on the KR1 and KR2 segment mixing line, but the data from Zone A and the Marie Byrd Land do not. All the data, however, plot below the SPRL and differ from those of the Indian and Pacific basins. **c**, The two mixing curves were calculated between the most enriched Hikurangi and the most depleted AAR (black dashed line) and PAR (grey dashed line) data, respectively, using the general mixing equation of Langmuir et al.<sup>54</sup>. We used unpublished Nd (7.19 ppm) and Hf (1.84 ppm) concentrations for AAR. For PAR, we inferred Nd (14.7 ppm) and Hf (3.83 ppm) concentrations from published data in PetDB. Hikurangi data are from Hoernle et al.<sup>32</sup> (Nd = 75.3 ppm and Hf = 11.5 ppm). **d**, The WARS and most of Zealandia are part of the mixing relationship with the KR1 and KR2 segments, whereas Hikurangi Seamounts and some of Zealandia and East Australia deviate from it. This deviation can be accounted for by contamination by the subcontinental lithosphere, which is often observed in volcanism from the initial stages of continental rifting<sup>32</sup>.

the Zealandia and Antarctica continents. In addition, the influence of any pre-existing lithospheric component would be eliminated by thermal erosion during rifting<sup>39</sup> or deep mantle upwelling<sup>14</sup>.

Further support for a deep source of the Zealandia–Antarctic Swell comes from seismic tomography. The isotopically defined

Zealandia–Antarctic domain corresponds to a widespread and deep province of low seismic velocities beneath the AAR (Fig. 6). The upper mantle (<250 km deep) below this region has low S-wave velocities<sup>40–42</sup>, which implies that it may be hotter than the neighbouring Pacific and Indian mantle domains. The shallow axial

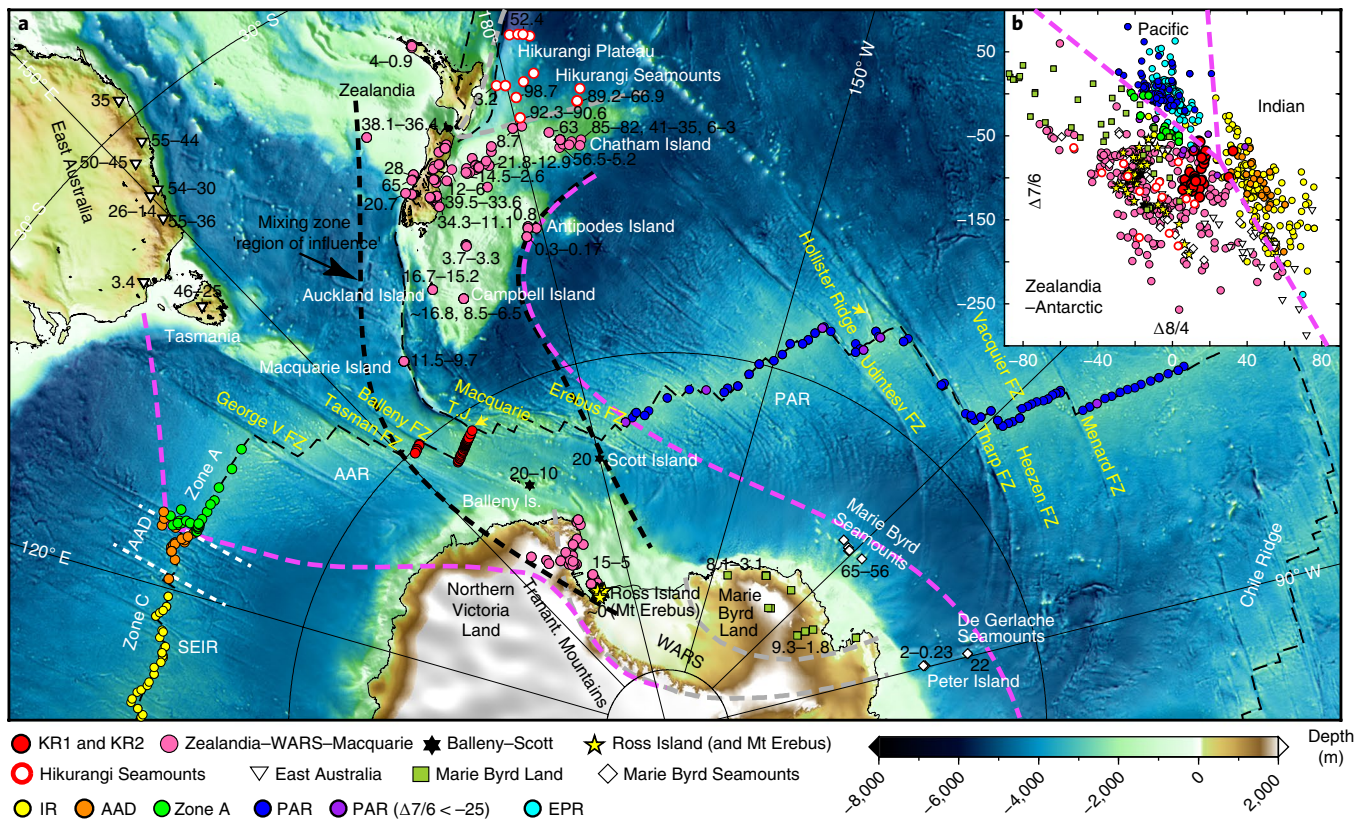


**Fig. 5 | Location of the Zealandia–Antarctic mantle domain. a**, Sample locations and domain boundaries. Circles show the sample locations of this study. Numbers around the circles, squares and triangles of the Cenozoic volcanoes erupted on the former Gondwana margin (pink, white and green) are the average ages (millions of years ago (Ma)) for each volcanic event. Note that the age distribution of volcanism is irregular, which implies that this volcanism cannot be explained by a single plume event<sup>24</sup>. The relatively young ages of the Cenozoic volcanism suggest geochemical signatures that correspond to their mantle source<sup>24</sup>. Furthermore, as the Antarctic Plate did not move significantly during the Cenozoic, the volcanic rocks from the Marie Byrd Seamounts and Balleny and Scott Islands provide a temporal perspective on the variations of the mantle source beneath this region<sup>14,36</sup>. The pink dashed lines show the proposed mantle domain boundaries among the Pacific (blue dots), Indian (yellow and gold dots) and Zealandia–Antarctic (red, pink, green and white dots) mantles. The thick black dashed line indicates the mixing zone in the middle of the Zealandia–Antarctic domain. The samples within this zone are part of the multi-isotopic mixing relationship discussed in the text. According to a tectonic reconstruction model<sup>36</sup>, Zealandia, Australia and Antarctica merged as the Gondwana margin and the Phoenix and Pacific plates were subducting beneath it prior to the break-up of Gondwana at ~90 Ma (refs. <sup>33,36,38</sup>). Around 90 Ma, the Hikurangi Plateau (area inside the grey dotted lines) on the Pacific Plate started to collide along the Pacific–Gondwana margin (the present Chatham Rise and Marie Byrd Land)<sup>32,38</sup>. Simultaneously, voluminous volcanic activity (Hikurangi Seamounts) occurred over the Hikurangi Plateau and Marie Byrd Land, which signalled the onset of a plume event with the arrival of a superplume head below the Pacific–Gondwana margin<sup>25,32,33,38</sup>. Thus, the Hikurangi Seamounts are considered to originate from the initial superplume event. The mixing relationship between Hikurangi and the KR1 and KR2 segments implies that the mantle domain may be traced back to the plume activity that caused the Gondwana break-up. **b**, In this discriminant diagram, the Zealandia–Antarctic, Pacific and Indian mantles are clearly clustered in  $\Delta 8/4$ – $\Delta 7/6$  space. The Zealandia–Antarctic mantle is divided into several domains, which include the mixing zone. The PAR data plotting in the Zealandia–Antarctic area (purple) are mostly from the region that extends from the Udintsev Fracture Zone (FZ) to the Heezen FZ, which was influenced by the Hollister Ridge.

depths of the KR1 and KR2 segments are also consistent with a hotter mantle beneath this region<sup>43</sup>. Similarly, the mantle below the WARS has isolated low P-wave<sup>44</sup> and S-wave<sup>14</sup> velocities ( $V_s$ ) down to a depth of ~1,200 km, apparently related to current Balleny/Ross Island volcanism. Mixing between plume components and depleted asthenosphere in the middle of the newly identified mantle domain (the mixing zone discussed above) may well be driven by the Balleny/Ross Island plume activity.

This model is broadly consistent with the concept of asthenospheric mixing induced by mantle upwelling<sup>34,35</sup>. Based on calculations of absolute plate motion and relative mantle plume strength, the plume-fed asthenosphere models<sup>34,35</sup> predict a 'region of influence' for the Balleny/Ross Island plume that covers at least the western extent of the newly proposed mixing zone. Deep mantle

upwellings would rise and mix with the shallower asthenospheric mantle, with some contamination by subcontinental lithospheric mantle where it is present.

### Domain boundaries and their significance

The new data demonstrate that the eastern boundary of the AAD is not the boundary between the Indian and Pacific mantle domains, as believed for the past three decades<sup>5–9</sup>. However, it remains the eastern boundary of the Indian Ocean mantle domain. It may be that the AAD today reflects an earlier boundary between the Pacific and Indian mantle regions, perhaps associated with subduction along the Gondwana margin. The break-up of Gondwana and the initiation of the Zealandia–Antarctic Swell created a new domain that separated the Pacific from the Indian mantle.

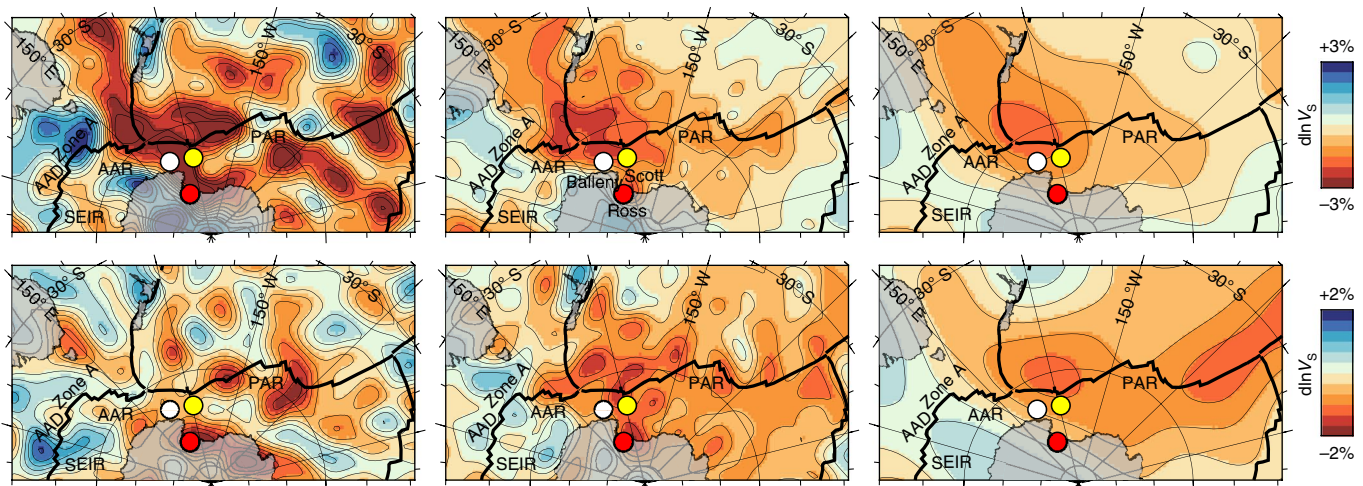


**Fig. 6 | Maps of shear-wave velocity variations  $d\ln V_s$  in the Southern Ocean.** Tomography models of SEMUCB-WM1 (left)<sup>55</sup>, S4ORTS (centre)<sup>40</sup> and SP12RTS (right)<sup>42</sup> at depths of 250 km (top) and 600 km (bottom) are compared. Three hotspots in the vicinity of the Southern Ocean mantle domain are denoted as circles: Balleny (white), Scott (yellow) and Ross (red) islands. The upper mantle anomalies in the Southern Ocean are consistently imaged by three tomography models and appear to be closely related with the Zealandia–Antarctic mantle domain. Moreover, the newly proposed mixing zone that may be driven by the Balleny/Ross Island plume activity coincides with the upper mantle  $V_s$  anomalies.

It mixed both east and west to create a mixed Pacific/Zealandia–Antarctic margin on the west adjacent to the AAD. In this context, the compositions sampled in Zone A are of particular interest. They form an intermediate field in radiogenic isotope space between the Pacific and Zealandia–Antarctic domains, which raises the possibility that the upwelling of Zealandia–Antarctic compositions might have mixed with the pre-existing Pacific mantle to create the distinctive composition observed in Zone A today. A full understanding of the distinct composition of Zone A, however, requires additional sampling between Zone A and the KR2 segment.

Although the current limited sampling along the west and east of the AAR does not allow a precise definition of the boundaries of the new mantle domain, it appears to be bounded by ancient, large-offset transform faults (Fig. 5). This feature is common to many mantle domains associated with hot spots. The North and South Atlantic basins, in particular, are separated by large equatorial transforms. For example, the Hayes Transform is the southern boundary of the influence of the Azores hot spot, and the Iceland hot spot is bounded by the large-offset Charlie–Gibbs Fracture Zone to the south<sup>45,46</sup> and the Tjörnes Fracture Zone to the north<sup>47</sup>. Similarly, the influence of the Galapagos plume has boundaries associated with ridge offsets<sup>48,49</sup>. Hence, there appears to be a clear association between major tectonic boundaries, bathymetry on the Earth's surface and the underlying upper mantle domains as reflected in the isotopic compositions of erupted basalts. This general phenomenon is further support for a deep origin of the Zealandia–Antarctic domain.

Collectively, these observations suggest a common origin for many of the world's mantle domains and their respective boundaries. Deep mantle upwellings feed and mix with upper mantle. These upwellings have distinctive histories and inherited isotopic compositions that are both old (Archaean and Proterozoic) and derived from the deep mantle where mixing is inefficient and large-scale heterogeneities therefore can be created and preserved for long periods of time. The upwellings mix with the asthenosphere at a level shallow enough that the flow and mixing end up bounded by shallow features in the upper mantle that are associated with major tectonic boundaries, such as large-offset transforms. This overall process then creates mantle domains bounded by large tectonic features near the surface. The implications are a

deep-seated, ancient origin for the enriched end members, with a flow and mixing shallow enough that the spatial extent of upwelling is constrained by tectonic features near the surface. Further tests of this overall framework can be undertaken by further sampling along the AAR and Southeast Indian Ridge to determine the exact nature and locations of the Zealandia–Antarctic domain boundaries.

### Online content

Any methods, additional references, Nature Research reporting summaries, source data, statements of data availability and associated accession codes are available at <https://doi.org/10.1038/s41561-018-0292-4>.

Received: 16 April 2018; Accepted: 17 December 2018;

Published online: 28 January 2019

### References

- Hofmann, A. W. in *Treatise on Geochemistry* 2nd edn, Vol. 3 (ed. Carlson, R. W.) 67–101 (Elsevier, Amsterdam, 2014).
- White, W. M. Probing the Earth's deep interior through geochemistry. *Geochem. Perspect.* **4**, 95–246 (2015).
- Hamelin, B. D. & Allègre, C. J. Large scale regional units in the depleted upper mantle revealed by an isotope study of the South-West Indian Ridge. *Nature* **315**, 196–199 (1985).
- Vlastélic, I. et al. Large-scale chemical and thermal division of the Pacific mantle. *Nature* **399**, 345–350 (1999).
- Kempton, P. D. et al. Sr–Nd–Pb–Hf isotope results from ODP Leg 187: evidence for mantle dynamics of the Australian–Antarctic Discordance and origin of the Indian MORB source. *Geochem. Geophys. Geosyst.* **3**, 1074 (2002).
- Hanan, B. B., Blichert-Toft, J., Pyle, D. G. & Christie, D. M. Contrasting origins of the upper mantle revealed by hafnium and lead isotopes from the Southeast Indian Ridge. *Nature* **432**, 91–94 (2004).
- Klein, E. M., Langmuir, C. H., Zindler, A., Staudigel, H. & Hamelin, B. Isotopic evidence of a mantle convection boundary at the Australian–Antarctic Discordance. *Nature* **133**, 623–629 (1988).
- Pyle, D. G., Christie, D. M., Mahoney, J. J. & Duncan, R. A. Geochemistry and geochronology of ancient southeast Indian and southwest Pacific seafloor. *J. Geophys. Res.* **100**, 22261–22282 (1995).
- Christie, D. M., West, B. P., Pyle, D. G. & Hanan, B. B. Chaotic topography, mantle flow and mantle migration in the Australian–Antarctic discordance. *Nature* **394**, 637–644 (1998).
- Gale, A., Dalton, C. A., Langmuir, C. H., Su, Y. & Schilling, J. G. The mean composition of ocean ridge basalts. *Geochem. Geophys. Geosyst.* **14**, 489–518 (2013).

11. Blichert-Toft, J. & White, W. M. Hf isotope geochemistry of the Galapagos Islands. *Geochem. Geophys. Geosyst.* **2**, 2000GC000138 (2001).
12. Hart, S. R. A large-scale isotope anomaly in the Southern Hemisphere mantle. *Nature* **309**, 753–757 (1984).
13. Sims, K. W. W. et al. A Sr, Nd, Hf, and Pb isotope perspective on the genesis and long-term evolution of alkaline magmas from Erebus volcano, Antarctica. *J. Volcanol. Geotherm. Res.* **177**, 606–618 (2008).
14. Phillips, E. H. et al. The nature and evolution of mantle upwelling at Ross Island, Antarctica, with implications for the HIMU source. *Earth Planet. Sci. Lett.* **498**, 38–53 (2018).
15. Rocholl, A., Stein, M., Molzahn, M., Hart, S. R. & Wörner, G. Geochemical evolution of rift magmas by progressive tapping of a stratified mantle source beneath the Ross Sea Rift, Northern Victoria Land, Antarctica. *Earth Planet. Sci. Lett.* **131**, 207–224 (1995).
16. Rocchi, S. et al. Cenozoic magmatism in the western Ross embayment: role of mantle plume versus plate dynamics in the development of the West Antarctic Rift system. *J. Geophys. Res.* **107**, 2195 (2002).
17. Nardini, I., Armienti, P., Rocchi, S., Dallai, L. & Harrison, D. Sr–Nd–Pb–He–O isotope and geochemical constraints on the genesis of Cenozoic magmas from the West Antarctic Rift. *J. Petrol.* **50**, 1359–1375 (2009).
18. Aviado, K. B., Rilling-Hall, S., Bryce, J. G. & Mukasa, S. B. Submarine and subaerial lavas in the West Antarctica Rift system: temporal record of shifting magma source components from the lithosphere and asthenosphere. *Geochem. Geophys. Geosyst.* **16**, 4344–4361 (2015).
19. Lanyon, R., Varne, R. & Crawford, A. J. Tasman tertiary basalts, the Balleny plume, and opening of the Tasman Sea (southwest Pacific Ocean). *Geology* **21**, 555–558 (1993).
20. Kamenetsky, V. S. & Maas, R. Mantle-melt evolution (dynamic source) in the origin of a single MORB suite: a perspective from magnesian glasses of Macquarie Island. *J. Petrol.* **43**, 1902–1922 (2002).
21. Hoernle, K. et al. Cenozoic intraplate volcanism on New Zealand: upwelling induced by lithospheric removal. *Earth Planet. Sci. Lett.* **248**, 350–367 (2006).
22. Panter, K. S. et al. The origin of HIMU in the SW Pacific: evidence from intraplate volcanism in southern New Zealand and subantarctic islands. *J. Petrol.* **47**, 1673–1704 (2006).
23. Timm, C., Hoernle, K., van den Boggard, P., Bindeman, I. & Weaver, S. Geochemical evolution of intraplate volcanism at Banks Peninsula, New Zealand: interaction between asthenospheric and lithospheric melts. *J. Petrol.* **50**, 989–1023 (2009).
24. Timm, C. et al. Temporal and geochemical evolution of the Cenozoic intraplate volcanism of Zealandia. *Earth Sci. Rev.* **98**, 38–64 (2010).
25. Hart, S. R., Blusztajn, J., LeMasurier, W. E. & Rex, D. C. Hobbs coast Cenozoic volcanism: implications for the West Antarctic Rift system. *Chem. Geol.* **139**, 223–248 (1997).
26. Panter, K. S., Hart, S. R., Kyle, P., Blusztajn, J. & Wilch, T. Geochemistry of Late Cenozoic basalts from the Crater Mountains: characterization of mantle sources in Marie Byrd Land, Antarctica. *Chem. Geol.* **165**, 215–241 (2000).
27. Frey, F. A., Green, D. H. & Roy, S. D. Integrated models of basalt petrogenesis: a study of quartz tholeiites to olivine melilitites from southeastern Australia utilizing geochemical and experimental petrological data. *J. Petrol.* **19**, 463–513 (1978).
28. O'Reilly, S. Y. & Zhang, M. Geochemical characteristics of lava-field basalts from eastern Australia and inferred sources: connections with the subcontinental lithospheric mantle? *Contrib. Mineral. Petrol.* **121**, 148–170 (1995).
29. Zhang, M. & O'Reilly, S. Y. Multiple sources for basaltic rocks from Dubbo, eastern Australia: geochemical evidence for plume–lithospheric mantle interaction. *Chem. Geol.* **136**, 33–54 (1997).
30. Zhang, M., O'Reilly, S. Y. & Chen, D. Location of Pacific and Indian mid-ocean ridge-type mantle in two time slices: evidence from Pb, Sr, and Nd isotopes for Cenozoic Australian basalts. *Geology* **27**, 39–42 (1999).
31. McBride, J. S., Lambert, D. D., Nicholls, I. A. & Price, R. C. Osmium isotopic evidence for crust–mantle interaction in the genesis of continental intraplate basalts from the newer volcanics province, southeastern Australia. *J. Petrol.* **42**, 1197–1218 (2001).
32. Hoernle, K. et al. Age and geochemistry of volcanic rocks from the Hikurangi and Manihiki oceanic plateaus. *Geochim. Cosmochim. Acta* **74**, 7196–7219 (2010).
33. Storey, B. C. et al. Mantle plumes and Antarctica–New Zealand rifting: evidence from Mid-Cretaceous mafic dykes. *J. Geol. Soc. Lond.* **156**, 659–671 (1999).
34. Yamamoto, M., Phipps Morgan, J. & Morgan, W. J. in *Plates, Plumes, and Planetary Processes* (eds Foulger, G. R. & Jurdy, D. M.) 165–188 (Geol. Soc. Am. Spec. Paper 430, Geological Society of America, 2007).
35. Yamamoto, M., Phipps Morgan, J., & Morgan, W. J. in *Plates, Plumes, and Planetary Processes* (eds Foulger, G. R. & Jurdy, D. M.) 189–208 (Geol. Soc. Am. Spec. Paper 430, Geological Society of America, 2007).
36. Seton, M. et al. Global continental and ocean basin reconstructions since 200 Ma. *Earth Sci. Rev.* **113**, 212–270 (2012).
37. Finn, C. A., Müller, R. D. & Panter, K. S. A Cenozoic diffuse alkaline magmatic province (DAMP) in the southwest Pacific without rift or plume origin. *Geochem. Geophys. Geosyst.* **6**, Q02005 (2005).
38. Kipf, A. et al. Seamounts off the West Antarctic margin: a case for non-hotspot driven intraplate volcanism. *Gondwana Res.* **25**, 1660–1679 (2014).
39. Larsen, H. C. et al. Rapid transition from continental breakup to igneous oceanic crust in the South China Sea. *Nat. Geosci.* **11**, 782–789 (2018).
40. Ritsema, J., Deuss, A., van Heijst, H. J. & Woodhouse, J. H. S40RTS: a degree-40 shear-velocity model for the mantle from new Rayleigh wave dispersion, teleseismic travel time and normal-mode splitting function measurements. *Geophys. J. Int.* **184**, 1223–1236 (2011).
41. French, S., Lekic, V. & Romanowicz, B. Waveform tomography reveals channelled flow at the base of the oceanic asthenosphere. *Science* **342**, 227–230 (2013).
42. Koelmeijer, P., Ritsema, J., Deuss, A. & van Heijst, H.-J. SP12RTS: a degree-12 model of shear- and compressional-wave velocity for Earth's mantle. *Geophys. J. Int.* **204**, 1024–1039 (2016).
43. Langmuir, C. H., Klein, E. M. & Plank, T. in *Mantle Flow and Melt Generation Beneath Ocean Ridges* (eds Morgan, J. P., Blackman, D. K. & Sinton, J. M.) 183–280 (Geophysical Monograph Series 71, American Geophysical Union, 1992).
44. Hansen, S. E. et al. Imaging the Antarctic mantle using adaptively parameterized P-wave tomography: evidence for heterogeneous structure beneath West Antarctica. *Earth Planet. Sci. Lett.* **408**, 66–78 (2014).
45. Schilling, J.-G. et al. Petrologic and geochemical variations along the Mid-Atlantic Ridge from 29°N to 73°N. *Am. J. Sci.* **283**, 510–586 (1983).
46. Langmuir, C. H. & Bender, J. F. The geochemistry of oceanic basalts in the vicinity of transform faults: observations and implications. *Earth Planet. Sci. Lett.* **69**, 107–127 (1984).
47. Blichert-Toft, J. A., Andres, A., Kingsley, M. R., Schilling, J.-G. & Albarède, F. Geochemical segmentation of the Mid-Atlantic Ridge north of Iceland and ridge–hot spot interaction in the North Atlantic. *Geochem. Geophys. Geosyst.* **6**, Q01E19 (2005).
48. Schilling, J.-G., Kingsley, R., Hanan, B. & McCully, B. Nd–Sr–Pb isotopic variations along the Gulf of Aden: evidence for the Afar mantle plume–lithosphere interaction. *J. Geophys. Res.* **97**, 10927–10966 (1992).
49. Canales, J. P., Ito, G., Detrick, R. S. & Sinton, J. Crustal thickness along the western Galapagos Spreading Center and the compensation of the Galapagos hotspot swell. *Earth Planet. Sci. Lett.* **203**, 311–327 (2002).
50. Schilling, J. G., Fontignie, D., Blichert-Toft, J., Kingsley, R. & Tomza, U. Pb–Hf–Nd–Sr isotope variations along the Galapagos Spreading Center (101–83°W): constraints on the dispersal of the Galapagos mantle plume. *Geochem. Geophys. Geosyst.* **4**, 8512 (2003).
51. Hanan, B. B. et al. Pb and Hf isotope variations along the Southeast Indian Ridge and the dynamic distribution of MORB source domains in the upper mantle. *Earth Planet. Sci. Lett.* **375**, 196–208 (2013).
52. Hamelin, C. et al. Geochemical portrayal of the Pacific Ridge: new isotopic data and statistical techniques. *Earth Planet. Sci. Lett.* **302**, 154–162 (2011).
53. Chauvel, C., Lewin, E., Carpentier, M., Arndt, N. T. & Marini, J.-C. Role of recycled oceanic basalt and sediment in generating the Hf–Nd mantle array. *Nat. Geosci.* **1**, 64–67 (2008).
54. Langmuir, C. H., Vocke, R. D. Jr, Hanson, G. N. & Hart, S. R. A general mixing equation with applications to Icelandic basalts. *Earth Planet. Sci. Lett.* **37**, 380–392 (1978).
55. French, S. W. & Romanowicz, B. Broad plumes rooted at the base of the Earth's mantle beneath major hotspots. *Nature* **525**, 95–99 (2015).

## Acknowledgements

This study was supported by KOPRI grant nos PP13040 and PE18050 to S.-H.P. Support at Harvard, Wyoming, Woods Hole and Tulsa was provided by the National Science Foundation (OCE1259916). J.B.-T. was supported by the French Agence Nationale de la Recherche through grant no. ANR-10-BLAN-0603 (M&Ms—Mantle Melting—Measurements, Models, Mechanisms). S.-S.K. was supported by Basic Science Research Program through the National Research Foundation of Korea (NRF) funded by the Ministry of Education (NRF-2017R1D1A1A02018632). J.L. was also supported by the CAS through grant no. Y4SL021001 and NSFC through grant no. 91628301. We thank the captain and crew of the icebreaker RV *Aaron* for support under difficult sea conditions. We appreciate the constructive reviews by J. Morgan and P. Kempton.

## Author contributions

S.-H.P. led the KOPRIDGE project, which included three cruises, interpreted the data and wrote the first draft of the manuscript. C.H.L. contributed to the initial stage of

cruise planning, geochemical interpretations and manuscript preparation and editing, and participated in the 2011 cruise. K.W.W.S. oversaw the isotopic analyses by S.R.S. and contributed to the geochemical interpretations and manuscript preparation and editing. J.B.-T. oversaw and participated in the Hf isotopic analyses by S.R.S. and contributed to the geochemical interpretations and manuscript preparation and editing. S.-S.K. contributed to the cruise design, performed geophysical data analyses and interpretations, and contributed to manuscript writing and editing. S.R.S. performed the Sr, Nd, Hf and Pb isotopic analyses and contributed to the table preparation, geochemical interpretations and manuscript editing. J.L. contributed to the cruise design, performed geophysical data analyses and interpretations, participated in the 2011 cruise and contributed to manuscript editing. H.C. and Y.-S.Y. contributed to the cruises and produced the relevant figures and maps. P.J.M. was involved in the cruise planning, geochemical interpretation and manuscript editing. All authors discussed the results and commented on the manuscript.

### Competing interests

The authors declare no competing interests.

### Additional information

**Supplementary information** is available for this paper at <https://doi.org/10.1038/s41561-018-0292-4>.

**Reprints and permissions information** is available at [www.nature.com/reprints](http://www.nature.com/reprints).

**Correspondence and requests for materials** should be addressed to S.-H.P.

**Publisher's note:** Springer Nature remains neutral with regard to jurisdictional claims in published maps and institutional affiliations.

© The Author(s), under exclusive licence to Springer Nature Limited 2019

## Methods

Samples were recovered by wax coring. Most samples are very fresh slightly phyrlic basaltic glasses. According to unpublished chemical data, all the samples are tholeiitic MORB.

**Sr, Nd and Pb isotopes.** Sr, Nd and Pb isotopic compositions were measured at the University of Wyoming High-Precision Isotope Laboratory using a ThermoFisher Scientific NEPTUNE Plus multicollector inductively coupled plasma mass spectrometer. Analyses were done on 1–2 mm basalt glass chips leached in 6 M HCl at 75 °C for 45 min to remove potential seawater precipitates or artefacts, then repeatedly rinsed in pure water. The efficacy of this leaching is discussed explicitly in the supplemental information of Sims et al.<sup>56</sup>. Samples were dissolved using a mixture of concentrated HF/HNO<sub>3</sub> followed by 6 M HCl. Pb was purified using standard anion exchange chromatography in HBr following Strelow and Toerien<sup>57</sup>. The bulk sample matrix was collected from the Pb purification procedure for analysis of Sr and Nd. Sr and rare earth element fractions were separated using a cation exchange column in HCl. The Sr and rare earth element fractions that contained Nd were subsequently purified using a SrSpec resin column and an LnSpec resin column, respectively.

Samples were dissolved in 5% HNO<sub>3</sub> solutions for all isotopic analyses. Samples were introduced into the plasma using either an Apex or Aridus II desolvating nebulizer. Sr isotopes were measured in the static mode using four Faraday collectors, with additional collectors used to monitor Rb and Kr interferences. Ratios were normalized to <sup>86</sup>Sr/<sup>88</sup>Sr = 0.1194 to correct for instrumental mass bias, and final data are reported relative to NBS987 <sup>87</sup>Sr/<sup>86</sup>Sr = 0.71024. Nd isotopes were measured in the static mode using seven Faraday collectors, with additional collectors used to monitor the Ce and Sm interferences. Ratios were normalized to <sup>146</sup>Nd/<sup>144</sup>Nd = 0.7219 to correct for instrumental mass bias, and final data are reported relative to La Jolla <sup>143</sup>Nd/<sup>144</sup>Nd = 0.51185. The total procedural blanks for Sr and Nd were <100 pg.

The United States Geological Survey (USGS) reference materials analysed as unknowns were used for quality assurance and to establish realistic estimates of the University of Wyoming's High Precision Laboratory's long-term reproducibility. The long-term reproducibility beginning in June 2013 until the present for BCR-2 is <sup>87</sup>Sr/<sup>86</sup>Sr = 0.705002 ± 0.000020 (2 s.d., *n* = 53) and <sup>143</sup>Nd/<sup>144</sup>Nd = 0.512634 ± 0.000012 (2 s.d., *n* = 14). Values for BCR-2 analysed during the AAR analytical sessions from February to December 2014 were <sup>87</sup>Sr/<sup>86</sup>Sr = 0.705006 ± 0.000013 (2 s.d., *n* = 6) and <sup>143</sup>Nd/<sup>144</sup>Nd = 0.512629 ± 0.000005 (*n* = 2). The long-term reproducibility beginning in October 2013 until the present for BHVO-2 is <sup>87</sup>Sr/<sup>86</sup>Sr = 0.703466 ± 0.000027 (2 s.d., *n* = 15) and <sup>143</sup>Nd/<sup>144</sup>Nd = 0.512981 ± 0.000010 (2 s.d., *n* = 30). Values for BHVO-2 analysed during the AAR analytical sessions from February to December 2014 were <sup>87</sup>Sr/<sup>86</sup>Sr = 0.703482 ± 0.000006 (*n* = 1) and <sup>143</sup>Nd/<sup>144</sup>Nd = 0.512985 ± 0.000006 (*n* = 3). The long-term reproducibility beginning in July 2014 until the present for BIR-1a is <sup>87</sup>Sr/<sup>86</sup>Sr = 0.703092 ± 0.000034 (2 s.d., *n* = 9) and <sup>143</sup>Nd/<sup>144</sup>Nd = 0.513089 ± 0.000017 (2 s.d., *n* = 4). Values for BIR-1a analysed during the AAR analytical sessions from February to December 2014 were <sup>87</sup>Sr/<sup>86</sup>Sr = 0.703102 ± 0.000053 (2 s.d., *n* = 3) and <sup>143</sup>Nd/<sup>144</sup>Nd = 0.513100 ± 0.000019 (*n* = 1). The long-term reproducibility beginning in March 2014 until the present for W-2a is <sup>87</sup>Sr/<sup>86</sup>Sr = 0.706983 ± 0.000024 (2 s.d., *n* = 6) and <sup>143</sup>Nd/<sup>144</sup>Nd = 0.512516 ± 0.000011 (2 s.d., *n* = 15). Values for W-2a analysed during the AAR analytical sessions from February to December 2014 were <sup>87</sup>Sr/<sup>86</sup>Sr = 0.706989 ± 0.000016 (*n* = 2) and <sup>143</sup>Nd/<sup>144</sup>Nd = 0.512513 ± 0.000009 (2 s.d., *n* = 4). These and additional values measured during the AAR analytical sessions and GEOREM values for the same USGS reference materials are given in Supplementary Table 2.

For the measurement of Pb isotopic compositions, Tl was added to each sample to correct for mass fractionation with a Pb/Tl ratio target of ~3/1. Pb and Tl isotopes were analysed in the static mode using six Faraday collectors with ratios normalized to <sup>203</sup>Tl/<sup>205</sup>Tl = 0.418922 to account for instrumental mass bias. A seventh Faraday collector was used to monitor Hg. Pb isotope ratios are reported relative to the NBS981 values of Thirlwall<sup>58</sup>. The total procedural blanks for Pb were <40 pg. The internal precisions for <sup>206</sup>Pb/<sup>204</sup>Pb, <sup>207</sup>Pb/<sup>204</sup>Pb and <sup>208</sup>Pb/<sup>204</sup>Pb were generally <60 ppm. Long-term reproducibility beginning in June 2013 until the present for BCR-2 is <sup>206</sup>Pb/<sup>204</sup>Pb = 18.7565 ± 0.0076, <sup>207</sup>Pb/<sup>204</sup>Pb = 15.6288 ± 0.0047, <sup>208</sup>Pb/<sup>204</sup>Pb = 38.7333 ± 0.0201, <sup>207</sup>Pb/<sup>206</sup>Pb = 0.83325 ± 0.00015 and <sup>208</sup>Pb/<sup>206</sup>Pb = 2.06505 ± 0.00085 (2 s.d., *n* = 21). Values for BCR-2 analysed during the AAR analytical sessions from February to December 2014 were <sup>206</sup>Pb/<sup>204</sup>Pb = 18.7660 ± 0.0411, <sup>207</sup>Pb/<sup>204</sup>Pb = 15.6286 ± 0.0068, <sup>208</sup>Pb/<sup>204</sup>Pb = 38.7570 ± 0.0822, <sup>207</sup>Pb/<sup>206</sup>Pb = 0.83282 ± 0.00099 and <sup>208</sup>Pb/<sup>206</sup>Pb = 2.06528 ± 0.00057 (2 s.d., *n* = 5). The long-term reproducibility beginning in June 2014 until the present for BHVO-2 is <sup>206</sup>Pb/<sup>204</sup>Pb = 18.6284 ± 0.0398, <sup>207</sup>Pb/<sup>204</sup>Pb = 15.5448 ± 0.0145, <sup>208</sup>Pb/<sup>204</sup>Pb = 38.2400 ± 0.0232, <sup>207</sup>Pb/<sup>206</sup>Pb = 0.83447 ± 0.00123 and <sup>208</sup>Pb/<sup>206</sup>Pb = 2.05278 ± 0.00182 (2 s.d., *n* = 7). Values for BHVO-2 analysed during the AAR analytical sessions from February to December 2014 were <sup>206</sup>Pb/<sup>204</sup>Pb = 18.5975 ± 0.0005, <sup>207</sup>Pb/<sup>204</sup>Pb = 15.5476 ± 0.0005,

<sup>208</sup>Pb/<sup>204</sup>Pb = 38.2165 ± 0.0013, <sup>207</sup>Pb/<sup>206</sup>Pb = 0.836006 ± 0.000010 and <sup>208</sup>Pb/<sup>206</sup>Pb = 2.054926 ± 0.000032 (*n* = 1). The long-term reproducibility beginning in June 2014 until the present for BIR-1a is <sup>206</sup>Pb/<sup>204</sup>Pb = 18.8580 ± 0.0042, <sup>207</sup>Pb/<sup>204</sup>Pb = 15.6654 ± 0.0030, <sup>208</sup>Pb/<sup>204</sup>Pb = 38.5111 ± 0.0106, <sup>207</sup>Pb/<sup>206</sup>Pb = 0.830705 ± 0.000014 and <sup>208</sup>Pb/<sup>206</sup>Pb = 2.042162 ± 0.000052 (2 s.d., *n* = 3). Values for BIR-1a analysed during the AAR analytical sessions from February to December 2014 were <sup>206</sup>Pb/<sup>204</sup>Pb = 18.8556 ± 0.0005, <sup>207</sup>Pb/<sup>204</sup>Pb = 15.6637 ± 0.0005, <sup>208</sup>Pb/<sup>204</sup>Pb = 38.5051 ± 0.0013, <sup>207</sup>Pb/<sup>206</sup>Pb = 0.830721 ± 0.000008 and <sup>208</sup>Pb/<sup>206</sup>Pb = 2.042105 ± 0.000026 (*n* = 1). The long-term reproducibility beginning in February 2014 until the present for W-2a is <sup>206</sup>Pb/<sup>204</sup>Pb = 18.7490 ± 0.0035, <sup>207</sup>Pb/<sup>204</sup>Pb = 15.6646 ± 0.0029, <sup>208</sup>Pb/<sup>204</sup>Pb = 38.6271 ± 0.0100, <sup>207</sup>Pb/<sup>206</sup>Pb = 0.83549 ± 0.00023 and <sup>208</sup>Pb/<sup>206</sup>Pb = 2.06022 ± 0.00067 (2 s.d., *n* = 4). Values for W-2a analysed during the AAR analytical sessions from February to December 2014 were <sup>206</sup>Pb/<sup>204</sup>Pb = 18.7481 ± 0.0013, <sup>207</sup>Pb/<sup>204</sup>Pb = 15.6643 ± 0.0013, <sup>208</sup>Pb/<sup>204</sup>Pb = 38.6280 ± 0.0034, <sup>207</sup>Pb/<sup>206</sup>Pb = 0.83551 ± 0.0001 and <sup>208</sup>Pb/<sup>206</sup>Pb = 2.06037 ± 0.00071 (*n* = 2). We estimate the long-term reproducibility of <sup>206</sup>Pb/<sup>204</sup>Pb, <sup>207</sup>Pb/<sup>204</sup>Pb and <sup>208</sup>Pb/<sup>204</sup>Pb at ~200–300 ppm based on these and other standard measurements. Reproducibilities for the <sup>208</sup>Pb/<sup>206</sup>Pb and <sup>207</sup>Pb/<sup>206</sup>Pb are correspondingly similar. All the USGS reference materials data described above and measured during the AAR analytical sessions, GEOREM values and additional literature values for the same USGS reference materials are given in Supplementary Table 2.

**Hf isotopes.** Hf isotopic compositions were measured at the Ecole Normale Supérieure de Lyon using a Nu Plasma high-resolution multicollector inductively coupled plasma mass spectrometer and following the protocol of Blichert-Toft et al.<sup>59</sup>. Analyses were done on 1–2 mm basalt glass chips leached in hot 6 M HCl to remove potential seawater precipitates or artefacts, and then repeatedly rinsed in pure water. Samples were dissolved in a 3:1 mixture of concentrated HF:HNO<sub>3</sub>, and then Hf was leached from the residue using concentrated HF. The samples were centrifuged and the HF solution, which contained Hf, decanted. The Hf fraction was purified using an anion-exchange column in HCl/HF and Hf collected with 6 M HCl followed by a cation-exchange column in HCl:H<sub>2</sub>O<sub>2</sub> and Hf collected with HCl:HF.

Samples were introduced into the plasma in 0.05 M HNO<sub>3</sub> for analysis of the Hf isotopic compositions. Hf isotopes were measured in the static mode using five Faraday collectors, with four additional collectors used to monitor the Lu, Yb, W and Ta isobaric interferences. Ratios were normalized to <sup>179</sup>Hf/<sup>177</sup>Hf = 0.7325, and repeat analysis of the JMC-475 Hf isotope standard gave <sup>176</sup>Hf/<sup>177</sup>Hf = 0.282167 ± 0.000016 (2 s.d., *n* = 51). The long-term reproducibility is ~20–30 ppm. The in-run errors were half that for all samples. Hafnium isotope data for USGS reference materials measured at the same time as the AAR samples are listed in Supplementary Table 2.

**Note on normalization.** Supplementary Table 3 provides standard analytical information for the data sets used here. These data show that it is not necessarily possible to renormalize all data to a single value due to differences in the 'standards' used for analysis and in some cases a lack of reported isotopic values obtained for such standards. We chose not to renormalize literature data for this reason. However, many of these data sets are highly important for our study and the comparison of isotopic compositions across ocean basins. The isotopic variation observed across these ocean basins is much greater (order of magnitude or greater) than the variation associated with different standard normalizations, and our interpretations based on the reported data are robust.

## Data availability

The authors declare that the data supporting the findings of this study are available in Supplementary Tables 1 and 2.

## References

- Sims, K. W. W. et al. Short length scale mantle heterogeneity beneath Iceland probed by glacial modulation of melting. *Earth Planet. Sci. Lett.* **379**, 146–157 (2013).
- Strelow, F. W. E. & Toerien, F. von S. Separation of lead(II) from bismuth(III), thallium(III), cadmium(II), mercury(II), gold(III), platinum(IV), palladium(II), and other elements by anion exchange chromatography. *Anal. Chem.* **38**, 545–548 (1966).
- Thirlwall, M. Multicollector ICP-MS analysis of Pb isotopes using a <sup>207</sup>Pb–<sup>204</sup>Pb double spike demonstrates up to 400 ppm/amu systematic errors in Tl-normalization. *Chem. Geol.* **184**, 255–279 (2002).
- Blichert-Toft, J., Chauvel, C. & Albarede, F. Separation of Hf and Lu for high-precision isotope analysis of rock samples by magnetic sector-multiple collector ICP-MS. *Contrib. Mineral. Petr.* **127**, 248–260 (1997).